

Fluorenone-based covalent organic frameworks with efficient exciton dissociation and well-defined active center for remarkable photocatalytic hydrogen evolution

Lei Hao^{a,1}, Rongchen Shen^{a,1}, Can Huang^a, Zizhan Liang^a, Neng Li^{b,*}, Peng Zhang^c, Xiužhi Li^d, Chaochao Qin^{d,*}, Xin Li^{a,*}

^a Institute of Biomass Engineering, Key Laboratory of Energy Plants Resource and Utilization, Ministry of Agriculture and Rural Affairs, South China Agricultural University, Guangzhou 510642, China

^b State Key Laboratory of Silicate Materials for Architectures, Wuhan University of Technology, Hubei 430070, China

^c State Centre for International Cooperation on Designer Low-Carbon & Environmental Materials (CDLCEM), School of Materials Science and Engineering, Zhengzhou University, Zhengzhou, Henan 450001, China

^d Henan Key Laboratory of Infrared Materials and Spectrum Measures and Applications, School of Physics, Henan Normal University, Xinxiang 453007, Henan, China



ARTICLE INFO

Keywords:

Covalent organic frameworks
Photocatalytic hydrogen evolution reaction
Fluorenone
Exciton dissociation
Charge dynamics

ABSTRACT

Precisely modulating both the fine structures and exciton behaviors of covalent organic framework (COF)-based photocatalysts for efficient photocatalytic hydrogen evolution is still a great challenge. Herein, we report two COFs, fluorenone-based COF (FOO-COF) and fluorenyl-based COF (FO-COF), for photocatalytic H₂ evolution. The results demonstrated that FOO-COF achieved a remarkable stability and hydrogen evolution rate of 119.1 mmol/h/g, surpassing those of many previously reported COF-based photocatalysts, thus resulting in an apparent quantum efficiency up to 20.5% at 435 nm. The joint observations from temperature-dependent photoluminescence, the delayed fluorescence and phosphorescence spectroscopy confirm that FOO-COF shows a stronger carrier separation and migration ability, much lower exciton binding energy, and faster dissociation speed of singlet and triplet excitons than FO-COF. More importantly, the femtosecond time-resolved transient absorption spectra (fs-TAS) revealed the great difference between the two COFs in electron trapping and exciton dissociation after Pt loading. Furthermore, theoretical calculations unveiled the feasibility of C=O groups in the LUMO sites of FOO-COF as active electronic centers for anchoring the photodeposited Pt cocatalysts, due to its much lower Gibbs free energy of hydrogen adsorption and more negative charge density. We believe that the introduction of C=O groups in the FOO-COF can act as both a dominant electronic collection center and partial active sites, which improve the D-A polarizability and boost the generation, separation, migration, and utilization of photogenerated carriers in the FOO-COF for achieving remarkable photocatalytic hydrogen evolution. The insights into the molecular-level mechanism in this work may guide the significance of the rational design of COF structures for advanced photocatalytic hydrogen evolution.

1. Introduction

Photocatalytic hydrogen evolution reaction is one of the ideal research directions for developing green hydrogen energy. Photocatalytic hydrogen production from water is a clean and sustainable energy-conversion approach to solving the increasing energy crisis and environmental challenges [1–3]. Recently, organic semiconductors have emerged as promising candidates for photocatalytic hydrogen

production because of their diverse chemical structures and highly tunable optoelectronic properties [4–8]. However, the structure-performance relationship in organic semiconductors for photocatalytic hydrogen evolution reaction is unclear [9]. Therefore, there are still some significant challenges in the rational design of high-efficiency organic semiconductors and the further improvement of the photocatalytic hydrogen evolution rate [10–13].

To date, covalent organic frameworks (COFs) have been widely used

* Corresponding authors.

E-mail addresses: lineng@whut.edu.cn (N. Li), qinchaochao@htu.edu.cn (C. Qin), Xinli@scau.edu.cn (X. Li).

¹ These authors contributed equally to this work.

in photocatalytic hydrogen evolution [14–17]. To realize highly photoactive COFs for efficient sunlight-driven H₂ conversion, many strategies have been developed to enhance the photon trapping ability and facilitate charge carrier separation, such as building D-A structures, using surface defects to load single atoms and surface functional group modification [3,17–19]. Conjugated polymers with sulfone building blocks and biphenyl-based COFs containing β -ethylene-cyano structures are also very promising in photocatalytic HER due to their hydrophilicity and excellent charge separation properties [20–23]. However, the high price and harsh synthesis conditions limit the further application of sulfone building blocks [24]. To address these issues, developing an efficient, stable, and inexpensive COF-based photocatalyst and gaining a deep understanding of its underlying photocatalytic mechanism remain the crucial challenges [25–27].

Fluorenone monomer, as a small molecule, is often used as an acceptor in organic semiconductors. When its 2,7-position is substituted with an electron donating group, the energy of the singlet excited state may be further reduced, while the absorption of redshift could be increased, due to the formation of stabilizing π , π^* state. At the same time, the charge transfer of π , π^* excited state will provide excessive electrons to carbonyl oxygen, making carbonyl more polar and alkaline. This is important for the adsorption of H* in the acidic sacrificial agents [27–30]. The presence of the middle carbonyl group has an electron-withdrawing effect on the benzene rings on both sides, which promotes the dipolarization of the entire fluorenone molecule. This can significantly promote the polarization distribution of electrons and holes within the COF, thus greatly enhancing the separation ability of photogenerated carriers [25,31]. We believe that fluorenone molecules as electron acceptor moieties in COFs have broad application prospects in photocatalytic hydrogen production. It can serve as an electron storage center in photocatalysis. However, no such work has been conducted to systematically investigate the roles of fluorenone sites and the structure-performance relationship in improving photocatalytic hydrogen production of COF-based photocatalysts.

With this objective, herein, we constructed FOO-COF by Schiff base reaction using fluorenone and one of the most common small molecules named 2,4,6-Triformylphloroglucinol (TP). For comparison, we prepared FO-COF with fluorene as the building block. Then, the photocatalytic hydrogen evolution reactions were performed. As a result, FOO-COF displayed a high hydrogen evolution rate up to 119.1 mmol h⁻¹ g⁻¹ with ascorbic acid as a sacrificial agent and Pt as cocatalysts under visible light irradiation, much higher than that of FO-COF (12.3 mmol h⁻¹ g⁻¹). The efficient exciton dissociation, improved charge separation and well-defined active center were further revealed by temperature-dependent photoluminescence, the delayed fluorescence and phosphorescence spectroscopy, the femtosecond time-resolved transient absorption spectra (fs-TAS) and density functional theory (DFT) calculations. This work has important guiding significance for developing highly efficient COFs to achieve large-scale application in photocatalytic hydrogen production.

2. Experimental section

2.1. Chemicals and materials

All chemicals and reagents were of analytical grade materials and used as received without further purification. The *o*-DCB (1,2-Dichlorobenzene, 99%), anhydrous *n*-BuOH (*n*-Butanol, 99.4%), Pyrrolidine (Py, 98%), Ascorbic acid (>99.0%), 2,7-Dinitro-9-fluorenone (>98%), 2,7-diaminofluorene (FO, 98%) were purchased from Macklin Chemicals. TP (2,4,6-Triformylphloroglucinol, 97%) was supplied by Jilin Chinese Academy of Sciences-Yanshen Technology Co. Ltd.

2.2. Synthesis of 2,7-diamino-9H-fluoren-9-one (FOO)

A stirred suspension of 2,7-dinitro-9-fluorenone (9.45 g, 35 mmol) in

ethanol (375 mL) was added into a solution of sodium sulfide nonahydrate (37.85 g, 157.5 mmol) and sodium hydroxide (15 g, 375 mmol) in water (650 mL). The mixture was heated at reflux for 5 h and left to stand overnight. The mixture was cooled to 0–5 °C and the resulting precipitate was collected by filtration. The crude product was washed successively with water (2 × 100 mL), aqueous NaOH (2 × 100 mL, 5% w/v), water (3 × 100 mL), cold EtOH (2 × 50 mL), ether (50 mL), and hexane (50 mL) and dried in vacuo. Recrystallization from acetone-ethanol (1:1 v/v) afforded the FOO (6.30 g, 86%) as purple needles.

2.3. Synthesis of FOO-COF and FO-COF

A Pyrex tube was charged with 2,4,6-trihydroxybenzene-1,3,5-tricarbaldehyde (16.8 mg, 0.08 mmol), 2,7-diamino-9 H-fluoren-9-one (25.0 mg, 0.12 mmol), *o*-1,2-Dichlorobenzene (0.75 mL), *n*-BuOH (0.25 mL), and Py (0.1 mL). This mixture was homogenized by sonication for 10 min and the tube was then flash frozen at 77 K (liquid N₂ bath) and degassed by three freeze-pump-thaw cycles and evacuated to an internal pressure of 100 m Torr. The tube was sealed off and then heated at 120 °C for 3 days. The brown precipitate was collected by centrifugation and washed with Tetrahydrofuran (100 mL) and anhydrous acetone (200 mL). After drying at 120 °C, the product was obtained as a black red powder (35 mg, 85%).

The synthetic route of FO-COF is basically the same as that of FOO-COF, in which the initial synthetic material 2,7-diamino-9 H-fluoren-9-one is replaced by 2,7-diaminofluorene, the product is red powder with a yield of 82%.

2.4. Photocatalytic hydrogen evolution

The photocatalytic water splitting reaction under visible-light irradiation was performed in a 250 mL Pyrex top-irradiation reaction vessel with a stationary temperature at 5 °C, which was connected to a glass closed gas system (Labsolar-6A, Perfect Light). In a typical process, 5 mg of the photocatalyst was dispersed in a Pyrex reaction cell with 100 mL 0.1 M ascorbic acid (AA) aqueous solution. The reaction cell was sealed and then irradiated with a 350 W Xe lamp (PLS-SXE300, Beijing Perfect Light Technology Co., Ltd, $\lambda > 420$ nm). During the photocatalytic reaction, the suspension was continuously stirred. The generated hydrogen was detected by GC-9500 online chromatograph.[32].

3. Results and discussion

3.1. Morphology and structure

FOO-COF and FO-COF (Fig. 1a) were synthesized through a Schiff-base condensation reaction of aromatic diamines with 1,3,5-triformylphloroglucinol. The irreversible keto-enol tautomerism occurs in these products, which enhances their chemical stability [33,34]. We used 2,7-diamino-9 H-fluoren-9-one (FOO) and 2,7-diaminofluorene (FO) as the monomer in a mixture of *o*-dichlorobenzene(*o*-DCB)/ *n*-Butanol (*n*-BuOH) (vol/vol, 3/1, 1 mL) at 120 °C for 3 days in the presence of pyrrolidine (Py) for preparation of FOO-COF and FO-COF, both of which are the nanocrystalline powder. The crystalline structures of FOO-COF and FO-COF were characterized by powder X-ray diffraction (XRD) measurements (Figs. 1b, 1c, 1d and 1e). In the region of 1.5–10°, both COFs exhibited various strong diffraction peaks corresponding to the hexagonal crystalline planes. FOO-COF displayed diffraction peaks at 3.42, 5.89, 6.86 and 9.03°, which were ascribed to the (100), (110), (200) and (120) crystal facets, respectively. To interpret the lattice information, the Pawley refinements of the experimental patterns gave the unit cell parameters of FOO-COF ($a = b = 29.80$ Å and $c = 7.32$ Å with the residual factors of $R_p = 4.70\%$ and $R_{wp} = 6.62\%$), FO-COF ($a = b = 29.80$ Å and $c = 7.30$ Å with the residual factors of $R_p = 4.02\%$ and $R_{wp} = 5.53\%$). Based on both the calculated diffraction patterns and experimental PXRD data, we propose that FOO-COF and FO-COF have

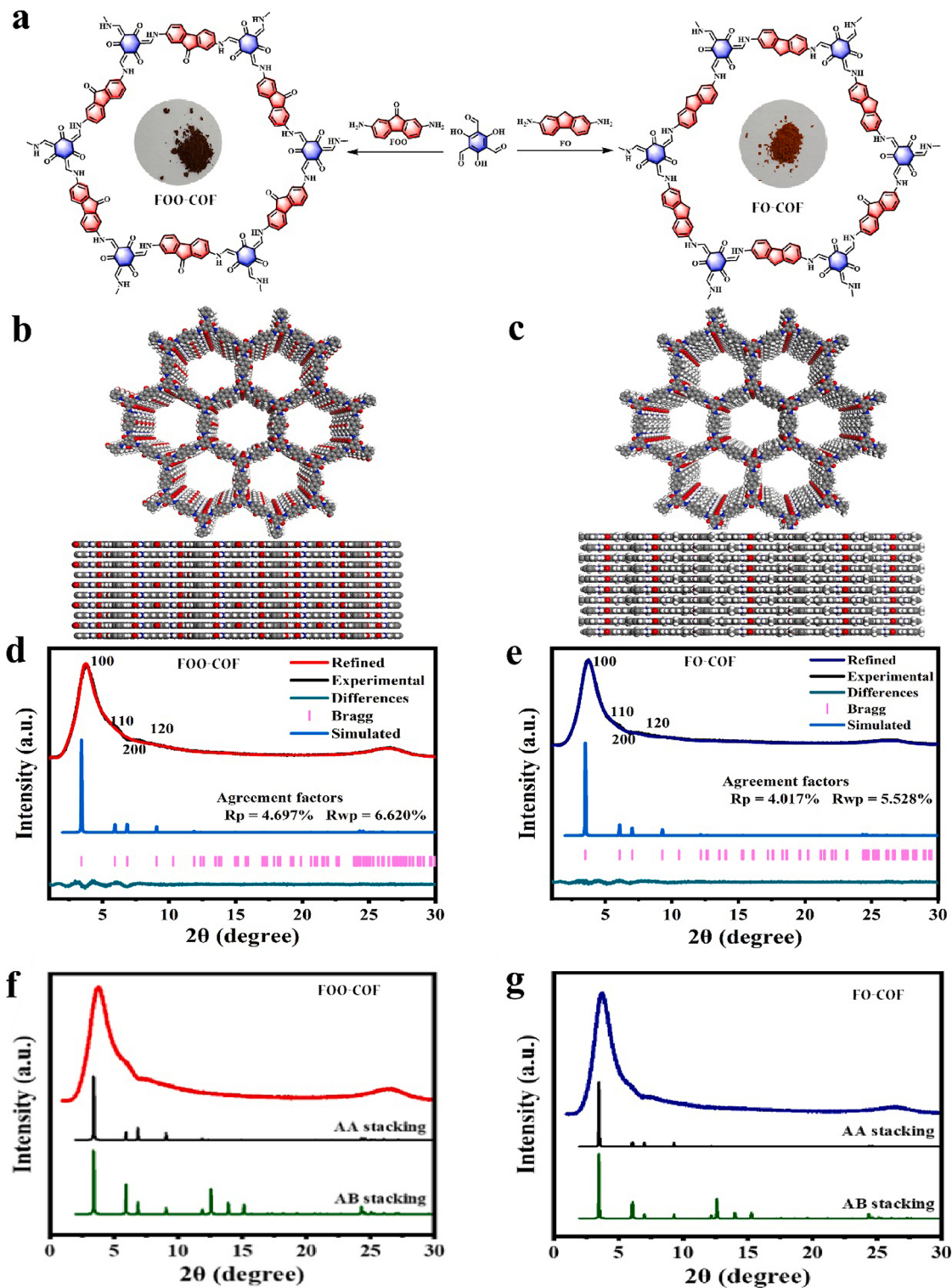


Fig. 1. (a) Schematic of the stepwise synthesis procedure of FOO-COF and FO-COF. (b), (c) Crystal structures of FOO-COF and FO-COF. Structural models for FOO-COF and FO-COF with perfectly eclipsed AA stacking patterns. (d), (e) Experimental diffraction patterns (black), profiles calculated from Le Bail fitting (pink) and residual (green), and pattern simulated from the structural model (AA Stacking) (blue) of FOO-COF and FO-COF. (f) experimental and simulated AA as well as AB stacking PXRD pattern of FOO-COF. (g) experimental and simulated AA as well as AB stacking PXRD pattern of FO-COF.

eclipsed (AA) layer stackings (Figs. 1f, 1g, 2a and 2d) rather than staggered (AB) stacking (Figs. 2b and 2e). Nitrogen sorption measurements are used to assess the porosity of FOO-COF and FO-COF at 77.0 K. Similarly, the Brunauer-Emmett-Teller (BET) surface area of FOO-COF ($1353.5 \text{ m}^2 \text{ g}^{-1}$) is smaller than that of FO-COF ($1665.5 \text{ m}^2 \text{ g}^{-1}$) due to the larger structure of building blocks. The sorption isotherms of

FOO-COF and FO-COF showed characteristic type-IV sorption isotherm curves, indicating a microporous feature. Nonlocal density functional theory (NLDFT) revealed that the pore diameter distribution of FOO-COF and FO-COF showed a significant peak centered at around 1.3 nm (Figs. 2c and 2f) [35].

The morphology of FOO-COF and FO-COF was further verified using

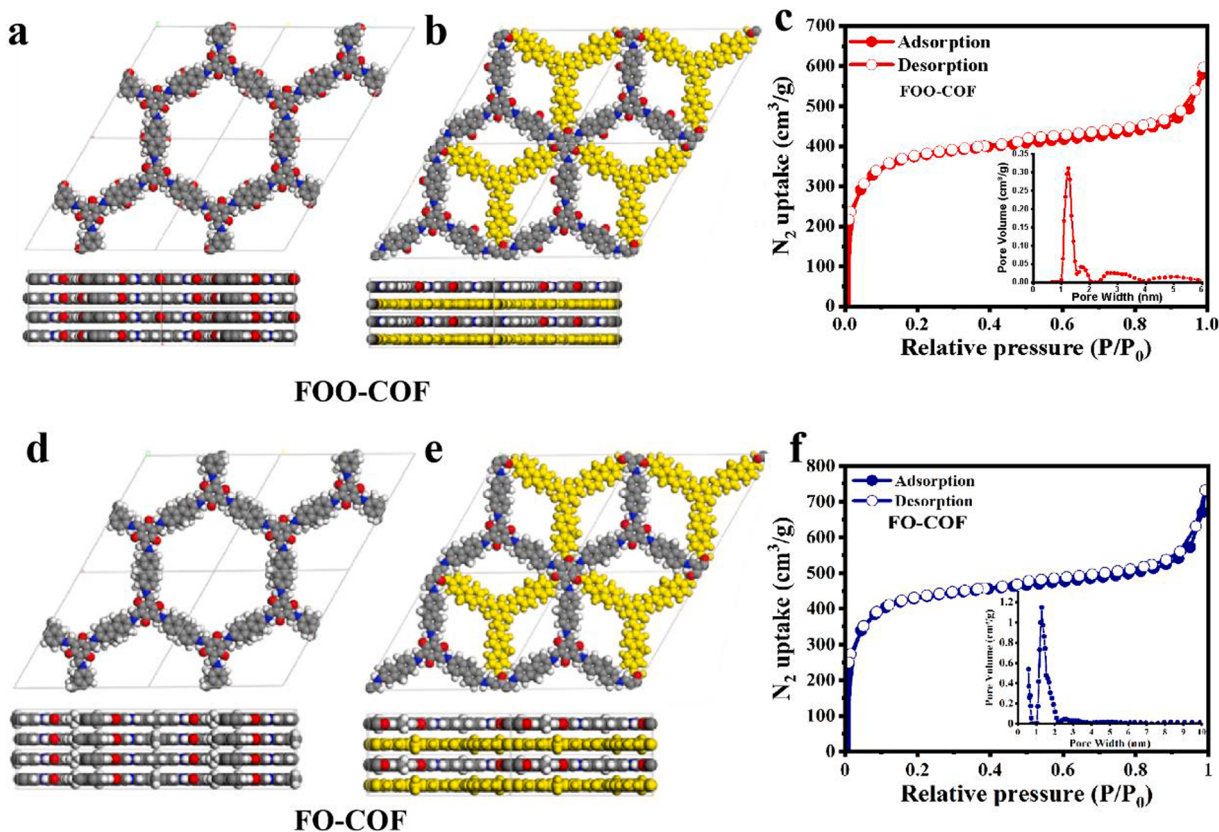


Fig. 2. (a) and (b) Side and top views of the possible crystal structures of the corresponding AA of FOO-COF as well as AB stacking. (c) The nitrogen adsorption (solid) and desorption (open) isotherms of FOO-COF. (d) and (e) Side and top views of the possible crystal structures of the corresponding AA of FO-COF as well as AB stacking. (f) The nitrogen adsorption (solid) and desorption (open) isotherms of FO-COF.

atomic force microscopy (AFM) (Figs. 3a–3f), scanning electron microscopy (SEM) (Fig. S1, S2) and TEM images (Figs. 3g and 3h), which showed sheet-shaped morphology with a thickness of 4.6 and 6.6 nm, respectively. The thinner thickness of FOO-COF may be due to the larger molecular structure of the monomer, which reduces the stacking rate of COF. This is also conducive to the photocatalytic hydrogen evolution performance of FOO-COF. The thermal stabilities of FOO-COF and FO-COF were confirmed by thermogravimetric analysis (TGA) (Fig. 3i), which indicated that both COFs could keep stable at temperatures below 400 °C.

3.2. Spectrum analysis, optical, and electronic properties

The chemical structure of the resulting FOO-COF and FO-COF were identified further by X-ray photoelectric (XPS) spectrum. High-resolution N 1 s X-ray photoelectric (XPS) spectrum of FOO-COF and FO-COF showed only one core binding energy peak at 399.8 eV, corresponding to the C–N groups (Fig. 4a). The binding energy peaks at 530.5 eV in the O 1 s XPS spectra of FOO-COF and FO-COF are assigned to C=O, while the binding energy peak of C-OH belongs to 532.0 eV. The binding energy peak at 533.5 eV belongs to the oxygen species adsorbed by the two materials (Fig. 4b). In the C1s XPS spectrum of FOO-COF and FO-COF, the core level peaks at 284.8, 285.9 and 289.0 eV corresponded to C=C, N-C and C=O bonds, respectively (Fig. 4c) [36,37]. These observations present evidences for the successful synthesis of β -ketoenamine-linked FOO-COF and FO-COF. Through further observation of the Fourier transform infrared (FT-IR) in Fig. 4d and Fig. S3, due to the conjugation, the ketone structure of Tp after keto-enol tautomerism transfers the absorption to a lower wave number below 1700 cm⁻¹, and the characteristic peak vibration band of C=O at 1605 cm⁻¹ further indicates the successful synthesis of the two

COF. Two new bands for FOO-COF and FO-COF were assigned to C=C and C–N groups, indicating the formation of covalent C–N bond and keto-enol tautomerization of the TP block. Furthermore, it could be observed from the ¹³C solid-state nuclear magnetic resonance (NMR) spectra of FOO-COF (Fig. 4e) that the characteristic peaks corresponding to the carbonyl C(a) (g) and secondary amine C(c), are located at 187.7 and 146.1 ppm, respectively. The other aromatic signals are located at 100–140 ppm. The carbon environment of FO-COF was almost similar to FOO-COF.

Before photocatalytic studies, the optical property of FOO-COF and FO-COF were also assessed using UV-vis diffuse reflectance spectrum (UV-Vis DRS) (Fig. 4f). Compared with the FO-COF, the FOO-COF exhibited a broader absorption band with an apparent redshift up to 730–780 nm due to the introduction of fluorenone groups. As shown in Fig. 4g, the bandgap (E_g) of FO-COF is 2.07 eV, much larger than that of FOO-COF (1.79 eV). [37] Such enhanced light absorption could be attributed to the conjugated donor-acceptor (D-A) structures with fluorenone acting as electron acceptors. We believe that introducing heteroatoms (O) could not only significantly reduce the band gap, but also cause a significant polarization effect on the fluorenone molecule [8,38,39]. This differs greatly from the FO-COF.

According to Mott-Schottky (MS) plots (at 0.1 M Na₂SO₄, pH 7) (Fig. S4a and S4b), both FOO-COF and FO-COF displayed positive slopes of the plots. The flat-band potentials (FBPs) of COFs could be roughly analogous to the bottom of the conduction band (CB) of COFs, and their FBPs were calculated vs. NHE. Obviously, the band levels show that both FOO-COF and FO-COF could meet the required thermodynamic conditions for photocatalytic HER (Fig. 4h). VB-XPS measurements (Fig. S4c and S4d) and ultraviolet photoelectron spectroscopy (UPS) were also conducted to study the band positions of FOO-COF and FO-COF (Fig. S5). The results of VB-XPS were consistent with those of

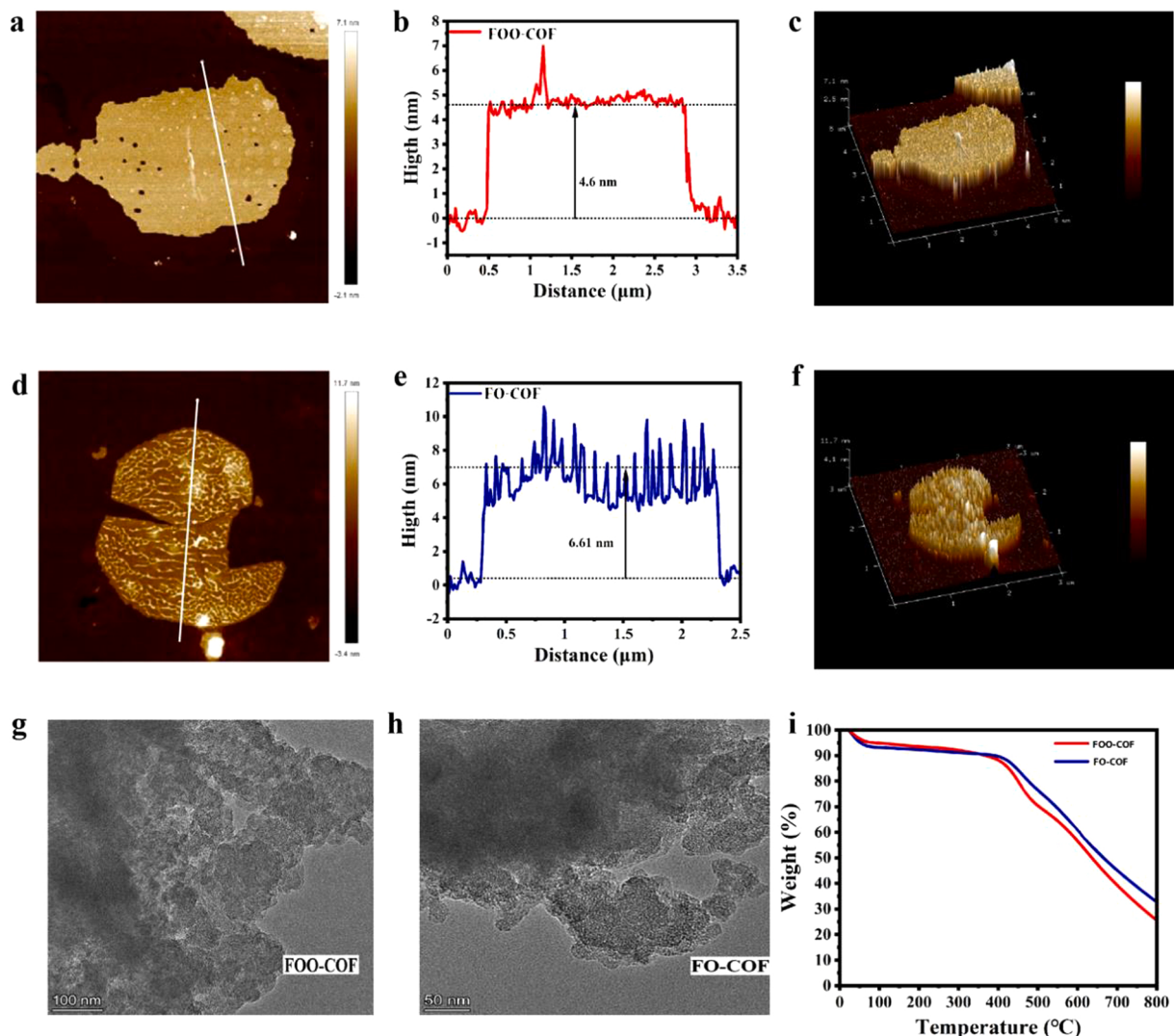


Fig. 3. AFM images of FOO-COF(a) Front Top View. (b) Side view (c) 3d image. AFM images of FO-COF (d) Front Top View. (e) Side view (f) 3d image. (g) and (h) TEM images of FOO-COF and FO-COF. (i) TGA of FOO-COF and FO-COF under N₂.

MS. In addition, the work function (ϕ) and E_{Vb} of FOO-COF and FO-COF can be estimated by the spectrogram of UPS. The ϕ of FOO-COF and FO-COF were calculated at 3.07 and 3.52 eV by subtracting the width of He I at an excitation energy of 21.22 eV. The E_{Vb} of FOO-COF and FO-COF were estimated to be 5.23 and 5.57 eV (vs. Vacuum), respectively. According to the reference standard, NHE (pH=7) equals a vacuum of 4.44 V. Thus, the VB potentials (vs. NHE) of FOO-COF and FO-COF were estimated to be 0.79 and 1.13 V, respectively. The FOO-COF exhibits the most negative lowest unoccupied molecular orbital (LUMO) potential, which could give the largest driving force for proton reduction, thus contributing to its highest photocatalytic H₂ evolution.

3.3. Photocatalytic hydrogen evolution performance

Encouraged by the above results, we tested the photocatalytic hydrogen-evolution activity of FOO-COF and FO-COF under visible light irradiation (Xe-lamp 350 W, $\lambda > 420$ nm) [40–43]. Fig. 5a shows the photocatalytic performance per unit mass of two COFs-based photocatalysts prepared. Notably, this is one of the highest performances of COF-based hydrogen evolution photocatalysts to date (Table S1). It can be found in Fig. 5b that the hydrogen evolution rates (HERs) of FOO-COF and FO-COF loaded Pt are 119.1 and 12.3 mmol/hg⁻¹, respectively. It is worth noting that even without Pt, FOO-COF also

shows a hydrogen evolution rate of up to 0.98 mmol/hg⁻¹, while no hydrogen is generated in FO-COF without Pt. In addition, we investigated the effects of the amount of cocatalyst and catalyst on the photocatalytic H₂ evolution. Due to the light shielding effect, the optimal amount of cocatalyst and catalyst for the two COFs is 3% Pt and 2 mg cat (Figs. 5c and 5f), respectively. In addition, many external factors, such as surface area, optical power density, photocatalyst quality, reactor temperature, etc., significantly affect the photocatalytic reaction rate. Here, we measured the photocatalytic performance per unit surface area, as shown in Fig. 5d. FOO-COF showed better photocatalytic performance. In addition, in order to understand the influence of different sacrificial agents on the hydrogen evolution performance of the two COFs, we tested four types of sacrificial agents. We found that the hydrogen evolution rate of the two COFs has a great relationship with the pH of the reaction solution. The acidic environment of ascorbic acid is more conducive to the photocatalytic hydrogen evolution reaction. In addition, no H₂ is generated when ethanol is used as a sacrificial agent (Fig. 5e). Furthermore, the influence of the concentration of sacrificial agents on the photocatalytic activity is also a factor worth considering. As shown in Fig. 5g, the photocatalytic performance of the two COFs does not increase linearly with the concentration of the sacrificial agent, which may be related to the threshold value of their photocatalytic rate. The stability test of the photocatalytic performance of FOO-COF was

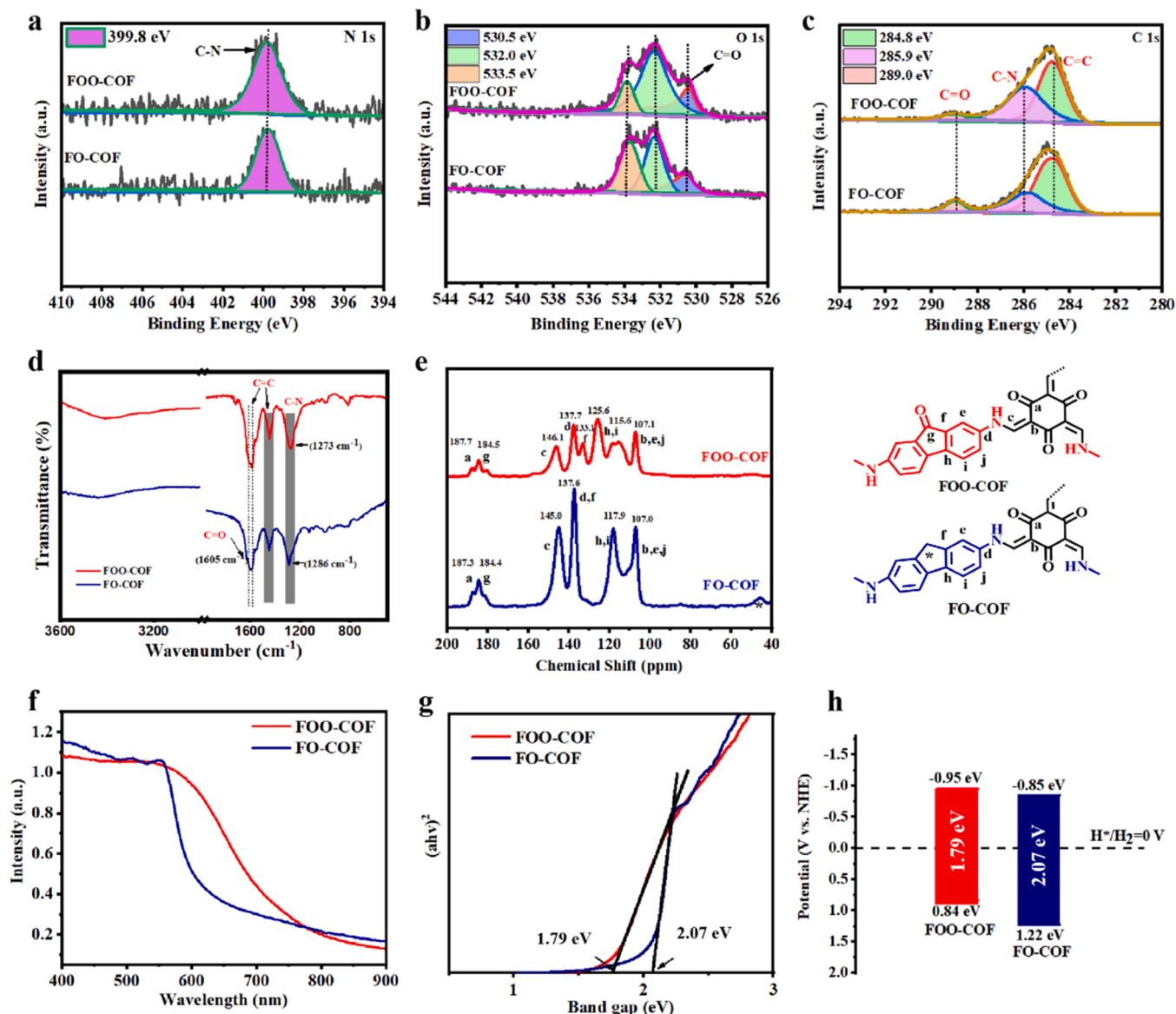


Fig. 4. XPS spectra of FOO-COF and FO-COF in the region of (a) N 1 s, (b) O 1 s, (c) C 1 s (d) FTIR spectra of FOO-COF and FO-COF. (e) Solid-state ¹³C NMR spectra of FOO-COF and FO-COF. (f) UV-vis absorption spectra of FOO-COF and FO-COF. (g) Tauc plots of FOO-COF and FO-COF. (h) Band structures of FOO-COF and FO-COF.

also carried out. As shown in the Fig. 5h, only 5% of the activity was lost after 8 cycles, which proves that FOO-COF has good photocatalytic stability. To quantify the wavelength-dependent photocatalytic performance of FOO-COF, the apparent quantum efficiency (AQE) was measured by a function of the proportion between the incident photonic numbers and the number of electrons utilized for H₂ formation (Fig. 5i). The AQE of FOO-COF is up to 20.5% at 435 nm [44]. These results demonstrate that the introduction of C=O on the FOO-COF framework significantly enhances the photocatalytic hydrogen-evolution activity. Water contact angles were also used to evaluate COF wettability of COFs (Fig. S6). Introducing fluorenone groups results in much smaller contact angles with pure water for FOO-COF (23.5°) in comparison with that of FO-COF (30.2°), indicating the improved hydrophilicity of the FOO-COF, which can contribute to the synergy between the multiple components and increasing the number of potential sites in an aqueous photocatalytic system [45]. In addition, the structure and composition of the two COFs remain unchanged before and after photocatalysis, which indicates that the two COFs have good stability (Figs. S7, 8, 9).

4. Photocatalytic mechanism analysis

Excitons dissociated into free charge carriers are also important for COFs-based photocatalysts. As displayed in Figs. 6a and 6b, we measured temperature-dependent photoluminescence spectrum (PL) to test the exciton binding energies. The intensity of PL for both FO-COF and FOO-COF decreased with increasing the temperature from 80 to 273 K, corresponding to the thermally activated nonradiative recombination process [46–49]. Subsequent fitting of these data by the following equation yielded a lower E_b (18.69 meV) for FOO-COF than that for FO-COF (34.55 meV) [50]. Where I₀ is the intensity at 0 K, E_b is the binding energy, A is a proportional constant and k_B is the Boltzmann constant.

$$I(T) = \frac{I_0}{1 + Ae^{-E_b/k_B T}}$$

This indicates that introducing C=O groups can reduce the exciton binding energy of FOO-COF and increase the carrier lifetime, thereby enhancing the photocatalytic hydrogen evolution capability.

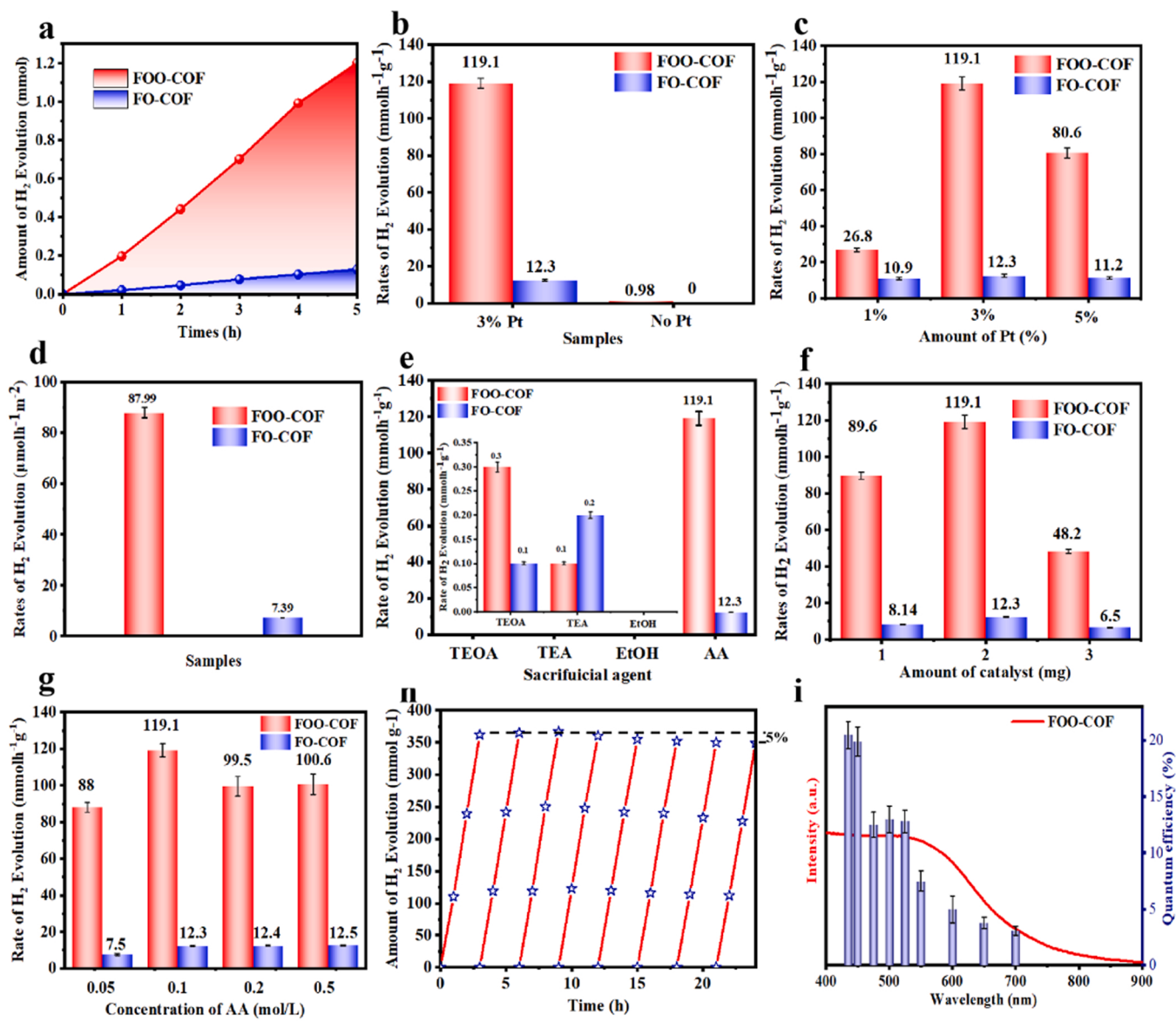


Fig. 5. (a) Hydrogen production rate under standard conditions (0.1 M AA 80 mL, 3% Pt, 2 mg catalyst). (b) Hydrogen evolution rate graph under standard conditions (with/without) Pt (3% Pt, 0.1 M AA 80 mL, 2 mg catalyst). (c) Hydrogen production rates with different amounts of cocatalyst (Pt) (2 mg catalyst, 0.1 M AA, 80 mL). (d) Hydrogen production rate per unit specific surface area (3% Pt, 0.1 M AA 80 mL, 2 mg catalyst). (e) Hydrogen production rate of different sacrificial agents (3% Pt, 0.1 M AA 80 mL). (f) Hydrogen production rates over different amounts of catalysts (3% Pt, 0.1 M AA 80 mL). (g) Hydrogen production rate over different concentrations of sacrificial agent (AA) (3% Pt, 2 mg catalyst, 80 mL water). (h) Photocatalytic durability test of FOO-COF (3 wt% Pt as cocatalyst and 0.1 M ascorbic acid 80 mL as a sacrificial reagent, 2 mg catalyst). (i) Wavelength-dependent AQE of photocatalytic H₂ production for FOO-COF.

Furthermore, to investigate the exciton signatures of two COF, the delayed fluorescence recorded at 300 K exhibited strong emission peaks at 634 and 695 nm (Fig. 6c). Compared with FO-COF, FOO-COF has a redshift and the peak intensity is significantly reduced. Since the radiation decay of singlet excitons causes delayed fluorescence in COF, the difference in peak intensity indicates a decreased amount of singlet excitons in FOO-COF [51]. The delayed fluorescence spectra monitored by the state emission peaks yielded mean radiative lifetimes of ~0.68 and ~0.86 ns for FOO-COF and FO-COF (Fig. 6c), respectively [52]. This result confirms that FOO-COF exhibits faster dissociation of singlet excitons than FO-COF, due to the smaller delayed fluorescence lifetime of FOO-COF. Delayed phosphorescence measurements were further performed to interrogate triplet excitons. Due to the spin-forbidden nature of triplet excitons, the delayed phosphorescence typically has a longer lifetime than the delayed fluorescence and thus can be distinguished from fluorescence spectra. As shown in Fig. 6d, the delayed

phosphorescence peak intensity of FOO-COF relative to FO-COF was significantly reduced, indicating a decreased concentration of triplet exciton. Estimated from the time-resolved delayed phosphorescence spectra, the delayed phosphorescence lifetimes of FO-COF and FOO-COF were ~11.86 and ~10.78 ms, respectively. The smaller delayed phosphorescence lifetime of FOO-COF indicates the faster dissociation of triplet excitons compared to that of FO-COF, which is consistent with the trend of singlet exciton dissociation for two COFs. Apparently, these results obtained from Figs. 6c and 6d, arrive at another important conclusion: FOO-COF can accelerate both the dissociation speed of singlet and triplet excitons [51], which could totally boost photocatalytic H₂ evolution. Apart from exciton dissociation, the charge-carrier concentration and migration rate in the catalyst are also important indicators to determine photocatalytic performance. Photoelectrochemical tests on the two COFs show that the slope of the Mott Schottky curve of FOO-COF is lower than that of FO-COF, which means

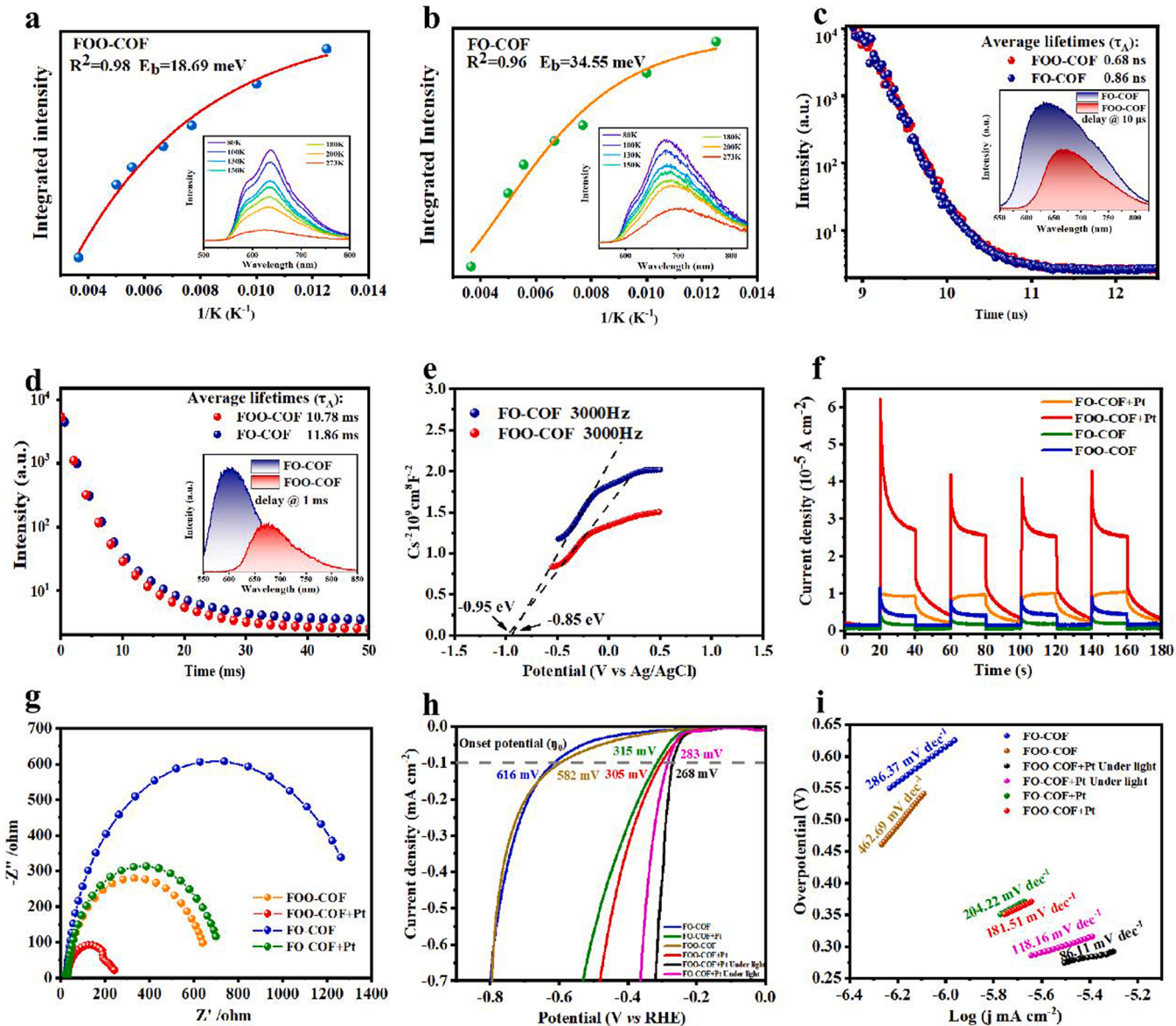


Fig. 6. Temperature-dependent photoluminescence spectrum of integrated PL intensity as a function of the temperature of (a) FOO-COF and (b) FO-COF (inset: temperature-dependent PL spectra from 80 to 273 K). (c) Time-resolved photoluminescence spectra of FOO-COF and FO-COF samples monitored (inset: Steady-state fluorescence spectra at a delayed time of 10 μs of FOO-COF and FO-COF at 300 K.). (d) Time-resolved phosphorescence spectra for FOO-COF and FO-COF samples (inset: Steady-state phosphorescence recorded at a delayed time of 1 ms for both FOO-COF and FO-COF samples). (e) Mott-Schottky curves for FOO-COF (blue) and FO-COF (red). (f) Transient photocurrent spectra of FOO-COF, FO-COF, FOO-COF, FO-COF+Pt and FOO-COF+Pt. (g) EIS Nyquist plots of FOO-COF, FO-COF, FOO-COF, FO-COF+Pt and FOO-COF+Pt. (h) LSV polarization curves and (i) Tafel plots of FOO-COF, FO-COF, FOO-COF+Pt and FOO-COF+Pt.

that higher charge concentration in FOO-COF is more conducive to the photocatalytic hydrogen evolution reaction (Fig. 6e) [53]. In order to further reveal the reason for the huge difference in the photocatalytic performance of the two COFs, we performed photocurrent and electrochemical impedance tests both before and after Pt loading. As expected, the photocurrent response density of FOO-COF before and after Pt loading is much higher than that of corresponding FO-COF (Fig. 6f) [54]. Nyquist curve of FOO-COF before and after Pt loading also shows a much smaller semicircular arc radius than that of corresponding FO-COF (Fig. 6g), indicating lower interfacial charge transfer resistance in FOO-COF loaded with Pt [55]. In addition, the intrinsic electrocatalytic activity and a number of active sites on the semiconductors are very crucial for photocatalytic hydrogen production. Accordingly, the polarization curves of the two COFs before and after Pt loading in 0.1 M H_2SO_4 show that the initial overpotential (305 mV) of FOO-COF+Pt is more active than that of FO-COF+Pt (315 mV), FOO-COF

(582 mV) and FO-COF (616 mV) (Fig. 6h), indicating the introduced Pt cocatalysts as active sites could significantly reduce the overpotentials. More importantly, the initial overpotentials of the two COFs are 283 (FO-COF+Pt) and 268 mV (FOO-COF+Pt), respectively, after being irradiated by an external light source. It is observed from its Tafel slope (Fig. 6i) that the slope of FOO-COF+Pt (86.11 mV dec $^{-1}$) is smaller than that in FO-COF+Pt (118.16 mV dec $^{-1}$) indicating more favorable HER kinetics. The decisive step for hydrogen evolution is Volmer step. It shows that this is a process of hydrogen production by adsorbing hydrogen protons [56]. The electrocatalytic experiments confirm that the FOO-COF has much more active sites, and the introduction of Pt could further increase the active sites and improve the intrinsic electrocatalytic activity.

The above results cannot reveal the real reason for the photocatalytic hydrogen evolution activity of the two kinds of COF from the intrinsic point of view. There are great differences in the photocatalytic activity

of the two COFs before and after Pt loading. To further investigate the advantages of fluorenone-based COF (FOO-COF) loaded with Pt in photoelectron separation and transfer in photocatalytic HER, femtosecond time-resolved transient absorption spectra (fs-TAS) measurements were conducted to evaluate the real-time relaxation kinetics of

photogenerated charge carriers [57,58]. Herein, we utilize a pump–probe configuration with a 365 nm pump and a white-light probe (440–700 nm) to track the photogenerated electron kinetics. Under 365 nm laser excitation, all the samples displayed a negative band at 450–650 nm, demonstrating the ground state bleach (GSB) (Figs. 7a, 7d,

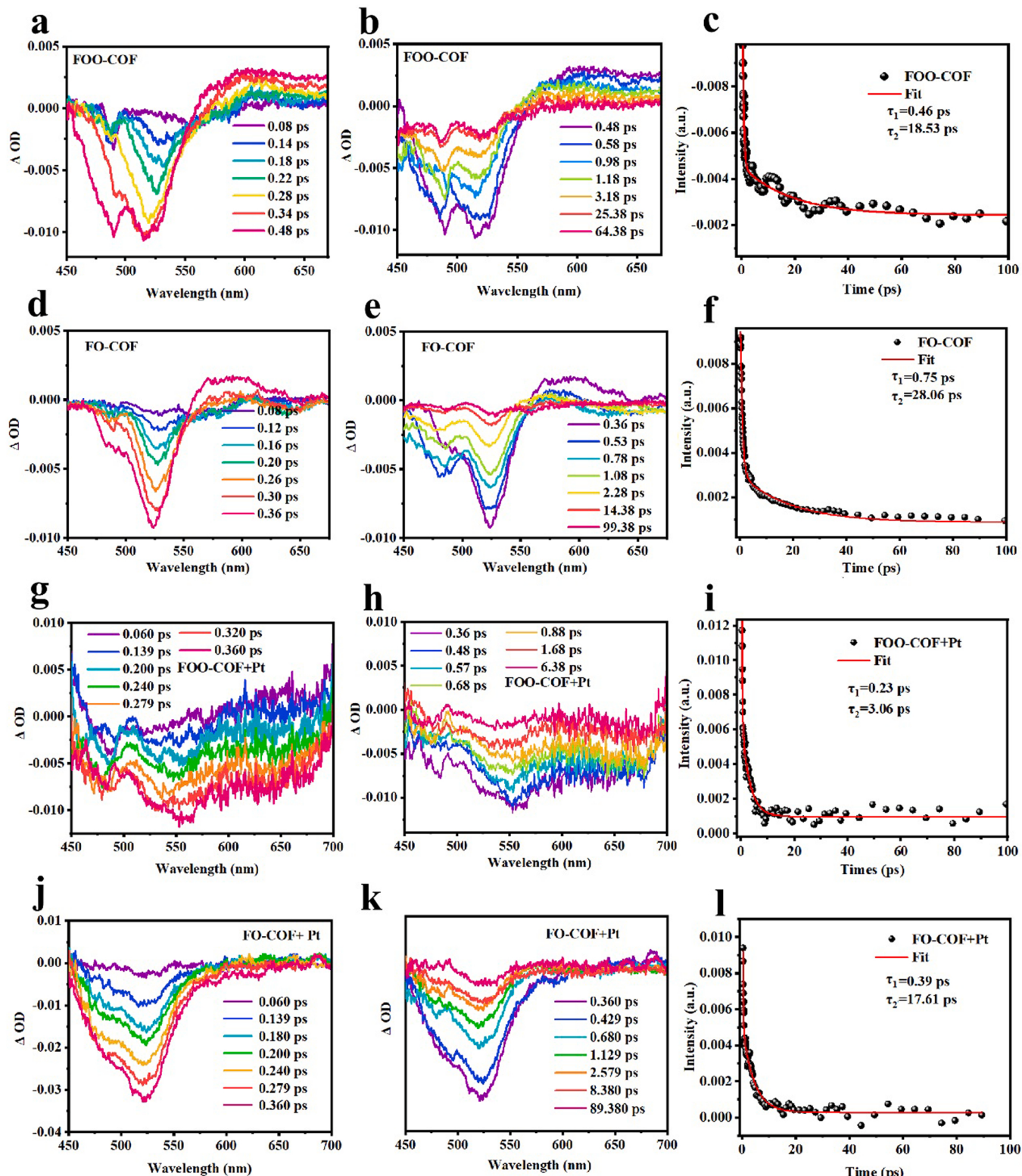


Fig. 7. Fs-TA spectra of (a), (b) FOO-COF, (d), (e) FO-COF, (g), (h) FOO-COF with 3%Pt. (j), (k) FO-COF with 3%Pt dispersed in ethylene glycol and excited at 365 nm. The decay kinetics were monitored at 524 nm of (c) FOO-COF, (f) FO-COF and (l) FO-COF with 3%Pt. (i) The decay kinetics monitored at 551 nm of FOO-COF with 3%Pt.

7g, 7j). The absorption intensity of FOO-COF and FO-COF increases gradually at 0.48 and 0.36 ps for the absorption near 524 nm (Figs. 7a and 7d). This characteristic corresponds to the process of excited electron relaxation to the bottom of the conduction band. When the electrons are excited from the VB to the CB and holes, remain at the VB, some of the excited electrons and holes will recombine with some fluorescence emission. At the same time, some other photogenerated electrons survive through an electron-trapping process. Due to the introduction of C=O sites, the fs-TAS spectra at 524 nm of FOO-COFs were different from the results of FO-COF. The electron-pulling property of C=O affects the fast recombination of electron-hole pairs in FOO-COF, which makes the characteristic peak of FO-COF decay more slowly at 524 nm (about 99.38 ps, Fig. 7e) than that of FOO-COF (about 64.38 ps, Fig. 7b). In addition, due to the fast recombination of photo-generated electron-hole pairs, the fs-TAS kinetics of FO-COF could be only fitted by biexponential decay processes ($\tau_1 = 0.75$ ps; $\tau_2 = 28.06$ ps) (Fig. 7f), which correspond to electron trapping and the efficient exciton dissociation, respectively. When introducing C=O into the

COF, the fs-TAS kinetics of FOO-COF could also be fitted well by a biexponential decay function ($\tau_1 = 0.46$ ps, $\tau_2 = 18.53$ ps) (Fig. 7c). The τ_1 of FOO-COF is a little smaller than the corresponding value of FO-COF, indicating the fast electron trapping in FOO-COF. The τ_2 for the FOO-COF is much shorter than that of FO-COFs due to the faster exciton dissociation induced charge separation in FOO-COFs. This also verifies the role of C=O for electron collection in the COF structure. As shown in Figs. 7i and 7j, after loading the Pt cocatalysts, FOO-COF+Pt ($\tau_2 = 3.06$ ps) and FO-COF+Pt ($\tau_2 = 17.61$ ps) displayed much shorter decay processes due to the intimate interaction and interfacial Schottky-junction between COF and Pt, which effectively suppresses the recombination of electron-hole pairs with ultrafast exciton dissociation and active electron injection from trap states to a metal center [59–62]. However, due to the existence of C=O structure, the characteristic peak of FOO-COF at 524 nm attenuates faster (Fig. 7h) than that of FO-COF (Fig. 7k) and the decay process is shorter. This indicates that the C=O structure in FOO-COF is optimally coordinated with Pt, which is able to collect electrons in large quantities and rapidly transfer them to Pt.

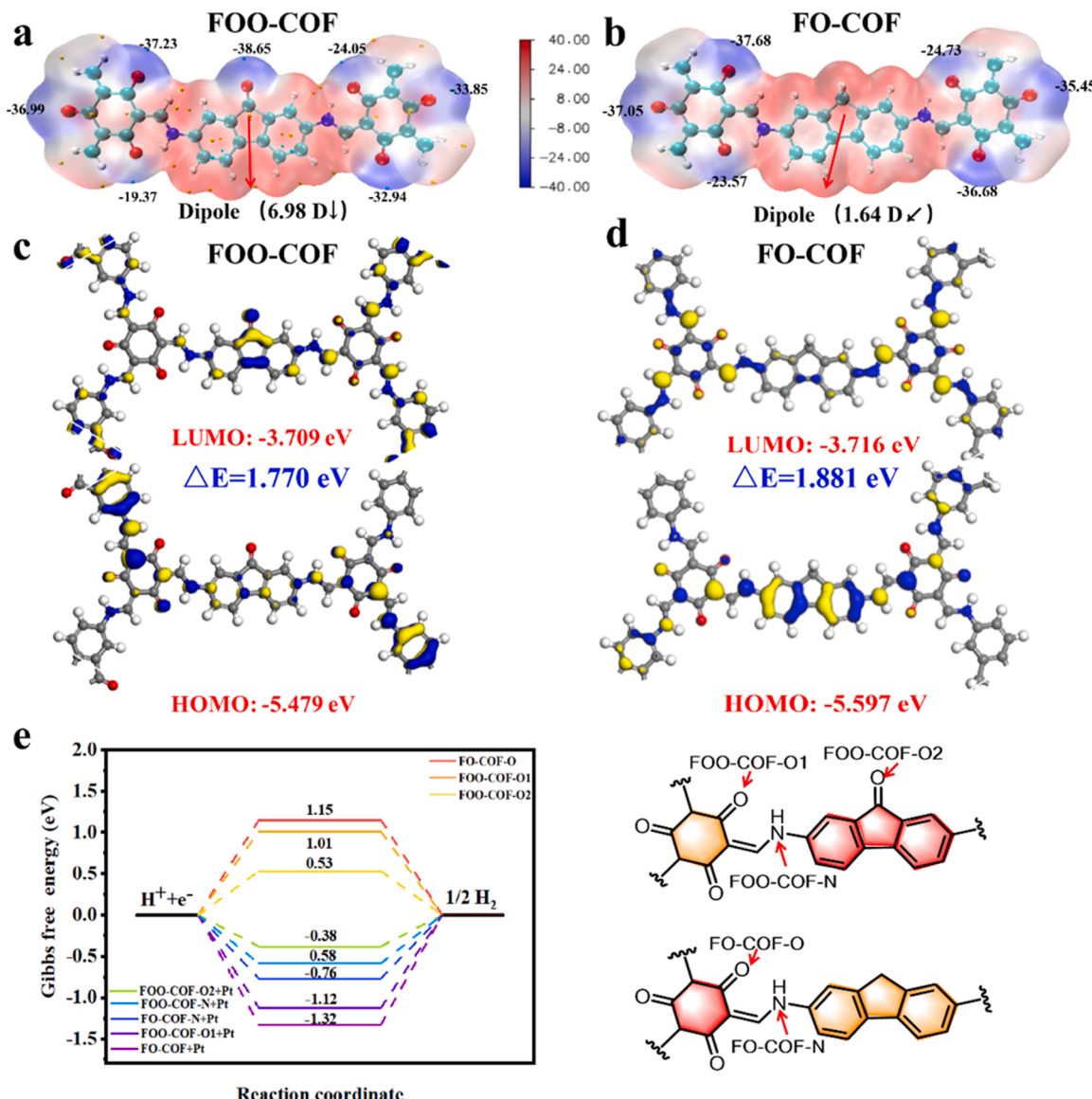


Fig. 8. The electrostatic potential (isosurface = 0.001 a.u.) of (a) Minimal Fragment Model of FOO-COF and (b) Minimal Fragment Model of FO-COF in the ground state, blue and red represented electron accumulation and depletion, respectively. (c) Frontier molecular orbitals and HOMO-LUMO energies of the smallest model unit of FOO-COF. (d) Frontier molecular orbitals and HOMO-LUMO energies of the smallest model unit of FO-COF. (e) Simulation of H⁺ adsorption at different positions of two COFs before and after Pt loading and schematic diagram of the different heteroatom positions in the two COFs.

To reveal the origin of FOO-COF's photoreactivity and electron transfer properties and find the real active center in FOO-COF, we used the quantum chemical method to calculate the static electronic distribution of the minimum fragment of the two COFs structures and analyze the number of charges through quantitative analysis (Figs. 8a, 8b) [63, 64]. The results show that the oxygen charge density of the carbonyl of fluorenone is higher than those in other positions. Moreover, FOO-COF has a larger dipole moment in the vector direction (about 6.98 D) than FO-COF (about 1.64 D), indicating that the larger polarization distribution of the electric field built in FOO-COF is more favorable for driving the charge transport within the catalyst. These results also provide further evidence that the carbonyl structure in FOO-COF serves as an electron collection center to facilitate photocatalytic hydrogen evolution reaction. To understand the photocatalyst mechanism, the frontier molecular orbitals (HOMO-LUMO) and energy levels of the smallest repeating units of FOO-COF and FO-COF are calculated by a well-defined density function theory (DFT) approach. The details of the DFT approach could be referred to as supporting information (SI). The results show that the calculated band gaps of the two COFs are 1.770 eV and 1.881 eV (Figs. 8c, 8d), respectively, which matches the experimental band gap well. The LUMO distribution results show that C=O of fluorenone in FOO-COF contributes more to LUMO, proving that C=O can be used as the photocatalytic active center. At the same time, the narrower band gap of FOO-COF obtained by calculation confirms that FOO-COF is more efficient for electron generation. Through density functional theory (DFT) calculation, the hydrogen evolution paths of FOO-COF and FO-COF were studied. Accordingly, the Gibbs free energy changes (ΔG) of hydrogen protons adsorbed by oxygen atoms and nitrogen atoms (positions) at different chemical positions in the two COFs before and after Pt loading were evaluated (Fig. 8e, S10, S11). The free energy of hydrogen adsorption showed a downward trend after loading Pt in different positions in the two COFs. Interestingly, the Gibbs free energy of adsorbed hydrogen protons after oxygen-supported Pt on fluorenone in FOO-COF is 0.38 eV (Fig. 8e), much lower than the Gibbs free energy of hydrogen protons adsorbed on the carbonyl oxygen and nitrogen atoms after the enol interconversion of the FOO-COF structure. This is consistent with the results of the previous electronic static distribution.

These results suggest that the modulation of fluorenone groups in FOO-COFs can effectively lower the energy barrier for hydrogen generation. The lower Gibbs free energy of hydrogen proton adsorption also

confirms the convenience of the fluorenone carbonyl group as the main electron collecting center and part of the active site (Fig. 9), which is consistent with the results of the above-mentioned photocatalytic experiments.

5. Conclusions

In summary, two imine-bonded COFs were synthesized and applied in photocatalytic hydrogen evolution, in which the FOO-COF achieved an astonishing hydrogen evolution efficiency of 119.1 mmol/h/g under visible light irradiation, surpassing those of many previously reported COF based photocatalysts, and resulting in an apparent quantum efficiency up to 20.5% at 435 nm. Compared with the FO-COF, we further demonstrate the importance of C=O as an electron collection center in COF in improving photocatalytic hydrogen evolution. The exciton behaviors of the two COFs were investigated by temperature-dependent photoluminescence, delayed fluorescence and phosphorescence spectroscopy. The generation and separation of charge carriers before and after Pt loading on two COFs were also compared by femtosecond time-resolved transient (fs-TAS) absorption spectroscopy and photoelectrochemical experiments. The results show that the C=O in the FOO-COF structure can accelerate the separation of photogenerated carriers and capture electrons quickly after loading Pt. The C=O structure can act as an electron collection center to transfer electrons to the Pt surface to participate in the reaction, thus fundamentally improving the photocatalytic hydrogen evolution capacity. The electrostatic potential distribution simulation of the smallest fragment of the two COFs suggests that the carbonyl group of fluorenone has the highest electron density, and the high delocalization of HOMO and LUMO, indicating the excellent electron transfer ability of FOO-COF. Density functional theory (DFT) calculations confirmed the excellent adsorption capacity of the carbonyl group of fluorenone for hydrogen protons after loading Pt. It is proved that fluorenone-based COFs have broad research and application value in photocatalytic hydrogen production, which lays the foundation for the design and synthesis of new COFs for photocatalytic hydrogen evolution.

CRediT authorship contribution statement

Lei Hao, Rongchen Shen, Can Huang, Zizhan Liang and Xin Li designed the systems, synthesized the photocatalysts, performed the

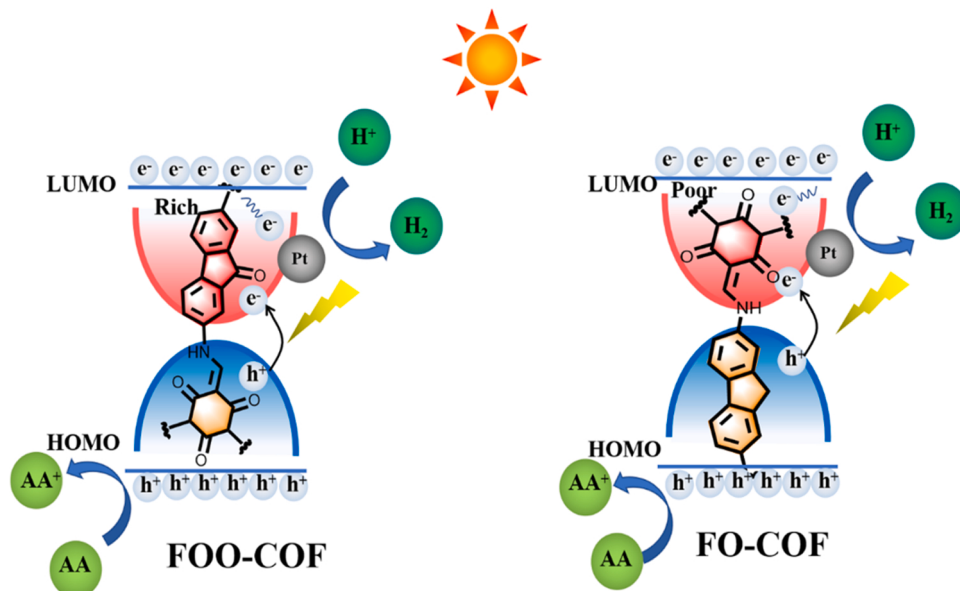


Fig. 9. Schematic diagram of photocatalytic hydrogen evolution of FOO-COF and FO-COF under standard conditions.

experimental measurement, analyzed the data as well as wrote the manuscript; Xiužhi Li, Chaochao Qin, carried out Transient absorption spectra experiments; Neng Li carried out the computational studies; Peng Zhang helped to revise the language of manuscript.

Declaration of Competing Interest

The authors declare that they have no known competing financial interests or personal relationships that could have appeared to influence the work reported in this paper.

Data availability

Data will be made available on request.

Acknowledgements

XL thanks National Natural Science Foundation of China (21975084, 51672089) and Natural Science Foundation of Guangdong Province (2021A1515010075) for their support.

Associated content

Supporting Information.

The Supporting Information is available free of charge.

Appendix A. Supporting information

Supplementary data associated with this article can be found in the online version at [doi:10.1016/j.apcatb.2023.122581](https://doi.org/10.1016/j.apcatb.2023.122581).

References

- [1] X. Li, J. Yu, M. Jaroniec, Hierarchical photocatalysts, *Chem. Soc. Rev.* 45 (2016) 2603–2636.
- [2] X. Li, J. Yu, M. Jaroniec, X. Chen, Cocatalysts for selective photoreduction of CO₂ into solar fuels, *Chem. Rev.* 119 (2019) 3962–4179.
- [3] P.Y. Dong, Y. Wang, A.C.J. Zhang, T. Cheng, X.G. Xi, J.L. Zhang, Platinum single atoms anchored on a covalent organic framework: boosting active sites for photocatalytic hydrogen evolution, *ACS Catal.* 11 (2021) 13266–13279.
- [4] L. Stegbauer, K. Schwinghammer, B.V. Lotsch, A hydrazone-based covalent organic framework for photocatalytic hydrogen production, *Chem. Sci.* 5 (2014) 2789–2793.
- [5] Z. Liang, R. Shen, Y.H. Ng, Y. Fu, T. Ma, P. Zhang, Y. Li, X. Li, Covalent organic frameworks: fundamentals, mechanisms, modification, and applications in photocatalysis, *Chem. Catal.* 2 (2022) 2157–2228.
- [6] R. Shen, L. Zhang, N. Li, Z. Lou, T. Ma, P. Zhang, Y. Li, X. Li, W.-N. Bonds, Precisely boost z-scheme interfacial charge transfer in g-C₃N₄/WO₃ heterojunctions for enhanced photocatalytic H₂ evolution, *ACS Catal.* (2022) 9994–10003.
- [7] C. Li, J. Liu, H. Li, K. Wu, J. Wang, Q. Yang, Covalent organic frameworks with high quantum efficiency in sacrificial photocatalytic hydrogen evolution, *Nat. Commun.* 13 (2022) 2357.
- [8] C. Zhao, Z. Chen, R. Shi, X. Yang, T. Zhang, Recent advances in conjugated polymers for visible-light-driven water splitting, *Adv. Mater.* 32 (2020) 1907296.
- [9] L. Wang, J. Liu, H. Wang, H. Cheng, X. Wu, Q. Zhang, H.J.S.B. Xu, Forming electron traps deactivates self-assembled crystalline organic nanosheets toward photocatalytic overall water splitting, *Sci. Bull.* 66 (2021) 265–274.
- [10] Y.O. Wang, A. Vogel, M. Sachs, R.S. Sprick, L. Wilbraham, S.J.A. Moniz, R. Godin, M.A. Zwijnenburg, J.R. Durrant, A.I. Cooper, J.W. Tang, Current understanding and challenges of solar-driven hydrogen generation using polymeric photocatalysts, *Nat. Energy* 4 (2019) 746–760.
- [11] H. Wang, H. Wang, Z. Wang, L. Tang, G. Zeng, P. Xu, M. Chen, T. Xiong, C. Zhou, X. Li, D. Huang, Y. Zhu, Z. Wang, J. Tang, Covalent organic framework photocatalysts: structures and applications, *Chem. Soc. Rev.* 49 (2020) 4135–4165.
- [12] V.S. Vyas, F. Haase, L. Stegbauer, G. Savascı, F. Podjaski, C. Ochsnerfeld, B. V. Lotsch, A tunable azine covalent organic framework platform for visible light-induced hydrogen generation, *Nat. Commun.* 6 (2015) 1–9.
- [13] Y. Guo, H. Li, W. Ma, W. Shi, Y. Zhu, W. Choi, Photocatalytic activity enhanced via surface hybridization, *Carbon Energy* 2 (2020) 308–349.
- [14] L. Stegbauer, S. Zech, G. Savascı, T. Banerjee, F. Podjaski, K. Schwinghammer, C. Ochsnerfeld, B.V. Lotsch, Tailor-made photoconductive pyrene-based covalent organic frameworks for visible-light driven hydrogen generation, *Adv. Energy Mater.* 8 (2018) 1703278.
- [15] Z.A. Lan, Y. Fang, X. Chen, X. Wang, Thermal annealing-induced structural reorganization in polymeric photocatalysts for enhanced hydrogen evolution, *Chem. Commun.* 55 (2019) 7756–7759.
- [16] J. Xiao, X. Liu, L. Pan, C. Shi, X. Zhang, J.-J. Zou, Heterogeneous photocatalytic organic transformation reactions using conjugated polymers-based materials, *ACS Catal.* 10 (2020) 12256–12283.
- [17] R. Shen, X. Li, C. Qin, P. Zhang, X. Li, Efficient photocatalytic hydrogen evolution by modulating excitonic effects in ni-intercalated covalent organic frameworks, *Adv. Energy Mater.* (2023) 2203695.
- [18] B.P. Biswal, H.A. Vignolo-Gonzalez, T. Banerjee, L. Grunenberg, G. Savascı, K. Gottschling, J. Nuss, C. Ochsnerfeld, B.V. Lotsch, Sustained solar H₂ evolution from a thiazolo[5,4-d]thiazole-bridged covalent organic framework and nickel-thiolate cluster in water, *J. Am. Chem. Soc.* 141 (2019) 11082–11092.
- [19] L.P. Guo, Y.L. Niu, S. Razzaque, B. Tan, S.B. Jin, Design of D-A(1)-A(2) covalent triazine frameworks via copolymerization for photocatalytic hydrogen evolution, *ACS Catal.* 9 (2019) 9438–9445.
- [20] W. Li, X. Huang, T. Zeng, Y.A. Liu, W. Hu, H. Yang, Y.B. Zhang, K. Wen, Thiazolo [5,4-d]thiazole-based donor-acceptor covalent organic framework for sunlight-driven hydrogen evolution, *Angew. Chem. Int. Ed.* 60 (2021) 1869–1874.
- [21] X. Wang, L. Chen, S.Y. Chong, M.A. Little, Y. Wu, W.H. Zhu, R. Clowes, Y. Yan, M. A. Zwijnenburg, R.S. Sprick, A.I. Cooper, Sulfone-containing covalent organic frameworks for photocatalytic hydrogen evolution from water, *Nat. Chem.* 10 (2018) 1180–1189.
- [22] Y. Bai, L. Wilbraham, H. Gao, R. Clowes, H. Yang, M.A. Zwijnenburg, A.I. Cooper, R.S. Sprick, Photocatalytic polymers of intrinsic microporosity for hydrogen production from water, *J. Mater. Chem. A* 9 (2021) 19958–19964.
- [23] C.M. Aitchison, M. Sachs, M.A. Little, L. Wilbraham, N.J. Brownbill, C.M. Kane, F. Blanc, M.A. Zwijnenburg, J.R. Durrant, R.S. Sprick, A.I. Cooper, Structure-activity relationships in well-defined conjugated oligomer photocatalysts for hydrogen production from water, *Chem. Sci.* 11 (2020) 8744–8756.
- [24] C. Li, J. Liu, H. Li, K. Wu, J. Wang, Q. Yang, Covalent organic frameworks with high quantum efficiency in sacrificial photocatalytic hydrogen evolution, *Nat. Commun.* 13 (2022) 2357.
- [25] N. Sun, D. Qi, Y. Jin, H. Wang, C. Wang, C. Qu, J. Liu, Y. Jin, W. Zhang, J. Jiang, Porous pyrene organic cage with unusual absorption bathochromic-shift enables visible light photocatalysis, *CCS Chem.* 4 (2022) 2588–2596.
- [26] S. Ghosh, A. Nakada, M.A. Springer, T. Kawaguchi, K. Suzuki, H. Kaji, I. Baburin, A. Kuc, T. Heine, H. Suzuki, R. Abe, S. Seki, Identification of prime factors to maximize the photocatalytic hydrogen evolution of covalent organic frameworks, *J. Am. Chem. Soc.* 142 (2020) 9752–9762.
- [27] G. Liu, J. Sheng, H. Wu, C. Yang, G. Yang, Y. Li, R. Ganguly, L. Zhu, Y. Zhao, Controlling supramolecular chirality of two-component hydrogels by J- and H-aggregation of building blocks, *J. Am. Chem. Soc.* 140 (2018) 6467–6473.
- [28] L. Hao, K.H. Huang, N.X. Wang, R.C. Shen, S.L. Chen, W.L. Bi, N. Li, P. Zhang, Y. J. Li, X. Li, Identifying the roles of imine and alkyne linkages in determining the photocatalytic hydrogen evolution over thiadiazole-based covalent organic frameworks, *Dalton Trans.* 51 (2022) 14952–14959.
- [29] L. Gilmanova, V. Bon, L. Shupletsov, D. Pohl, M. Rauche, E. Brunner, S. Kaskel, Chemically stable carbazole-based imine covalent organic frameworks with acidochromic response for humidity control applications, *J. Am. Chem. Soc.* 143 (2021) 18368–18373.
- [30] D. Bessinger, L. Ascherl, F. Auras, T. Bein, Spectrally switchable photodetection with near-infrared-absorbing covalent organic frameworks, *J. Am. Chem. Soc.* 139 (2017) 12035–12042.
- [31] Z. Mi, P. Yang, R. Wang, J. Unruangsri, W.L. Yang, C.C. Wang, J. Guo, Stable radical cation-containing covalent organic frameworks exhibiting remarkable structure-enhanced photothermal conversion, *J. Am. Chem. Soc.* 141 (2019) 14433–14442.
- [32] B. Hu, T.L. Liu, Tanking up energy through atypical charging, *Science* 372 (2021) 788–789.
- [33] G. Xing, W. Zheng, L. Gao, T. Zhang, X. Wu, S. Fu, X. Song, Z. Zhao, S. Osella, M. Martínez-Abadía, Nonplanar rhombus and kagome 2D covalent organic frameworks from distorted aromatics for electrical conduction, *J. Am. Chem. Soc.* 144 (2022) 5042–5050.
- [34] Y. Tang, W. Zhou, Q. Shang, Y. Guo, H. Hu, Z. Li, Y. Zhang, L. Liu, H. Wang, X. Tan, T. Yu, J. Ye, Discerning the mechanism of expedited interfacial electron transformation boosting photocatalytic hydrogen evolution by metallic 1T-WS₂-induced photothermal effect, *Appl. Catal. B Environ.* 310 (2022), 121295.
- [35] J. Yuan, X. You, N.A. Khan, R. Li, R. Zhang, J. Shen, L. Cao, M. Long, Y. Liu, Z. Xu, H. Wu, Z. Jiang, Photo-tailored heterocrystalline covalent organic framework membranes for organics separation, *Nat. Commun.* 13 (2022) 3826.
- [36] A.C. Sedgwick, L. Wu, H.-H. Han, S.D. Bull, X.-P. He, T.D. James, J.L. Sessler, B. Z. Tang, H. Tian, J. Yoon, Excited-state intramolecular proton-transfer (ESIPT) based fluorescence sensors and imaging agents, *Chem. Soc. Rev.* 47 (2018) 8842–8880.
- [37] Y. Zhao, H. Liu, C. Wu, Z. Zhang, Q. Pan, F. Hu, R. Wang, P. Li, X. Huang, Z. Li, Fully conjugated two-dimensional sp₂-carbon covalent organic frameworks as artificial photosystem I with high efficiency, *Angew. Chem. Int. Ed.* 131 (2019) 5430–5435.
- [38] X. Ma, G. Wang, L. Qin, J. Liu, B. Li, Y. Hu, H. Cheng, Z-scheme g-C₃N₄-AQ-MoO₃ photocatalyst with unique electron transfer channel and large reduction area for enhanced sunlight photocatalytic hydrogen production, *Appl. Catal. B Environ.* 288 (2021), 120025.
- [39] Z. Liang, R. Shen, T. Ma, P. Zhang, Y. Li, N. Li, X. Li, All-organic covalent organic frameworks/perylene diimide urea polymer S-Scheme photocatalyst for boosted H₂ generation, *Chin. J. Catal.* (2022), 220618.
- [40] W.-K. An, S.-J. Zheng, X. Xu, L.-J. Liu, J.-S. Ren, L. Fan, Z.-K. Yang, Y. Ren, C. Xu, Integrating benzofuran and heteroradialene into donor-acceptor covalent organic

- frameworks for photocatalytic construction of multi-substituted olefins, *Appl. Catal. B Environ.* 316 (2022), 121630.
- [41] B. Bonillo, R.S. Sprick, A.I. Cooper, Tuning photophysical properties in conjugated microporous polymers by comonomer doping strategies, *Chem. Mater.* 28 (2016) 3469–3480.
- [42] R.S. Sprick, L. Wilbraham, Y. Bai, P. Guiglion, A. Monti, R. Clowes, A.I. Cooper, M. A. Zwijnenburg, Nitrogen containing linear poly(phenylene) derivatives for photocatalytic hydrogen evolution from water, *Chem. Mater.* 30 (2018) 5733–5742.
- [43] S. Cao, L. Piao, Considerations for a more accurate evaluation method for photocatalytic water splitting, *Angew. Chem. Int. Ed.* 59 (2020) 18312–18320.
- [44] M. Qureshi, K. Takanabe, Insights on measuring and reporting heterogeneous photocatalysis: efficiency definitions and setup examples, *Chem. Mater.* 29 (2017) 158–167.
- [45] Z. Wang, T. Hisatomi, R. Li, K. Sayama, G. Liu, K. Domen, C. Li, L. Wang, Efficiency accreditation and testing protocols for particulate photocatalysts toward solar fuel production, *Joule* 5 (2021) 344–359.
- [46] M. Melchionna, P. Fornasiero, Updates on the roadmap for photocatalysis, *ACS Catal.* 10 (2020) 5493–5501.
- [47] F. Yu, Z. Zhu, S. Wang, J. Wang, Z. Xu, F. Song, Z. Dong, Z. Zhang, Novel donor-acceptor-acceptor ternary conjugated microporous polymers with boosting forward charge separation and suppressing backward charge recombination for photocatalytic reduction of uranium (VI), *Appl. Catal. B Environ.* 301 (2022), 120819.
- [48] X.Y. Wang, L.J. Chen, S.Y. Chong, M.A. Little, Y.Z. Wu, W.H. Zhu, R. Clowes, Y. Yan, M.A. Zwijnenburg, R.S. Sprick, A.I. Cooper, Sulfone-containing covalent organic frameworks for photocatalytic hydrogen evolution from water, *Nat. Chem.* 10 (2018) 1180–1189.
- [49] C. Li, J. Liu, H. Li, K. Wu, J. Wang, Q. Yang, Covalent organic frameworks with high quantum efficiency in sacrificial photocatalytic hydrogen evolution, *Nat. Commun.* 13 (2022) 1–9.
- [50] J. Xu, C. Yang, S. Bi, W. Wang, Y. He, D. Wu, Q. Liang, X. Wang, F. Zhang, Vinylene-linked covalent organic frameworks (COFs) with symmetry-tuned polarity and photocatalytic activity, *Angew. Chem. Int. Ed. Engl.* 59 (2020) 23845–23853.
- [51] L. Lin, Z. Lin, J. Zhang, X. Cai, W. Lin, Z. Yu, X. Wang, Molecular-level insights on the reactive facet of carbon nitride single crystals photocatalysing overall water splitting, *Nat. Catal.* 3 (2020) 649–655.
- [52] J. Zhang, Y. Yang, H. Deng, U. Farooq, X. Yang, J. Khan, J. Tang, H. Song, High quantum yield blue emission from lead free inorganic antimony halide perovskite colloidal quantum dots, *Acs Nano* 11 (2017) 9294–9302.
- [53] F. Liu, Y. He, X. Liu, Z. Wang, H.-L. Liu, X. Zhu, C.-C. Hou, Y. Weng, Q. Zhang, Y. Chen, Regulating excitonic effects in covalent organic frameworks to promote free charge carrier generation, *ACS Catal.* (2022) 9494–9502.
- [54] H. Wang, X. Sun, D. Li, X. Zhang, S. Chen, W. Shao, Y. Tian, Y. Xie, Boosting hot-electron generation: exciton dissociation at the order disorder interfaces in polymeric photocatalysts, *J. Am. Chem. Soc.* 139 (2017) 2468–2473.
- [55] H. Wang, D. Yong, S. Chen, S. Jiang, X. Zhang, W. Shao, Q. Zhang, W. Yan, B. Pan, Y. Xie, Oxygen-vacancy-mediated exciton dissociation in BiOBr for boosting charge-carrier-involved molecular oxygen activation, *J. Am. Chem. Soc.* 140 (2018) 1760–1766.
- [56] H. Wang, X.S. Sun, D.D. Li, X.D. Zhang, S.C. Chen, W. Shao, Y.P. Tian, Y. Xie, Boosting hot-electron generation: exciton dissociation at the order disorder interfaces in polymeric photocatalysts, *J. Am. Chem. Soc.* 139 (2017) 2468–2473.
- [57] D. Liang, J. Wu, C. Xie, J. Wen, Y. Lyu, Z. Sofer, J. Zheng, S. Wang, Efficiently and selectively photocatalytic cleavage of CC bond by C₃N₄ nanosheets: defect-enhanced engineering and rational reaction route, *Appl. Catal. B Environ.* 317 (2022), 121690.
- [58] S. Cao, B. Shen, T. Tong, J. Fu, J. Yu, 2D/2D heterojunction of ultrathin MXene/Bi₂WO₆ nanosheets for improved photocatalytic CO₂ reduction, *Adv. Funct. Mater.* 28 (2018) 1800136.
- [59] C. Cheng, B. He, J. Fan, B. Cheng, S. Cao, J. Yu, An inorganic/organic S-scheme heterojunction H₂-production photocatalyst and its charge transfer mechanism, *Adv. Mater.* 33 (2021) 2100317.
- [60] D.H.K. Murthy, H. Matsuzaki, Z. Wang, Y. Suzuki, T. Hisatomi, K. Seki, Y. Inoue, K. Domen, A. Furube, Origin of the overall water splitting activity of Ta₃N₅ revealed by ultrafast transient absorption spectroscopy, *Chem. Sci.* 10 (2019) 5353–5362.
- [61] Z. Yan, W. Wang, L. Du, J. Zhu, D.L. Phillips, J. Xu, Interpreting the enhanced photoactivities of 0D/1D heterojunctions of CdS quantum dots/TiO₂ nanotube arrays using femtosecond transient absorption spectroscopy, *Appl. Catal. B Environ.* 275 (2020), 119151.
- [62] J. Bai, R. Shen, Z. Jiang, P. Zhang, Y. Li, X. Li, Integration of 2D layered CdS/WO₃ S-scheme heterojunctions and metallic Ti₃C₂ MXene-based Ohmic junctions for effective photocatalytic H₂ generation, *Chin. J. Catal.* 43 (2022) 359–369.
- [63] H. Ben, G. Yan, H. Liu, C. Ling, Y. Fan, X. Zhang, Local spatial polarization induced efficient charge separation of squaraine-linked COF for enhanced photocatalytic performance, *Adv. Funct. Mater.* 32 (2022) 2104519.
- [64] L.-W. Luo, W. Ma, P. Dong, X. Huang, C. Yan, C. Han, P. Zheng, C. Zhang, J.-X. Jiang, Synthetic control of electronic property and porosity in anthraquinone-based conjugated polymer cathodes for high-rate and long-cycle-life Na-organic batteries, *ACS Nano* (2022) 14590–14599.